

# Long-Range Thermal 3D Perception in Low Contrast Environments

Filippov, Andrey  
andrey@elphel.com  
+1(801)783-5555x106

Filippova, Olga  
olga@elphel.com  
+1(801)783-5555x107

Elphel, Inc. 1455 West 2200 South #205, West Valley City, UT 84119, USA



## NASA SBIR 2021-I Phase I Final Report November 19, 2021

### Abstract

This report discusses the results of Phase I effort to prove the feasibility of dramatic improvement of the microbolometer-based **Long Wave Infrared (LWIR)** detectors sensitivity, especially for the 3D measurements. The resulting low **SWaP-C** thermal depth-sensing system will enable the situational awareness of Autonomous Air Vehicles for **Advanced Air Mobility (AAM)**. It will provide robust 3D information of the surrounding environment, including low-contrast static and moving objects, at far distances in degraded visual conditions and **GPS**-denied areas. Our multi-sensor 3D perception enabled by **COTS** uncooled thermal sensors mitigates major weakness of **LWIR** sensors - low contrast by increasing the system sensitivity over an order of magnitude.

There were no available thermal image sets suitable for evaluating this technology, making datasets acquisition our first goal. We discuss the design and construction of the prototype system with sixteen  $640\text{pix} \times 512\text{pix}$  **LWIR** detectors, camera calibration to subpixel resolution, capture, and process synchronized image. The results show the  $3.84\times$  contrast increase for intrascene-only data and an additional  $5.5\times$  - with the interscene accumulation, reaching system **noise-equivalent temperature difference (NETD)** of 1.9 mK with the 40 mK sensors.

# Contents

Contents	2
List of Figures	2
1 Project Summary	3
1.1 Identification and Significance of Innovation	3
1.2 List of Technical Objectives	3
1.3 List of Technical Accomplishments	3
1.4 Name and Address of Principal Investigator	3
1.5 Name and Address of Offeror	3
2 Abstract	4
3 Technical Objectives	4
3.1 Approach	4
4 Technical Activities	5
4.1 Multi-Sensor Camera Assembly and Testing	5
4.2 Camera Calibration	5
4.3 Field Image Acquisition	6
4.4 Extending Software to Support Arbitrary Number of Sensors	8
4.5 Generating a Single-Scene Disparity Map	8
4.6 Generating a Disparity Map from a Scene Sequence	9
4.7 Evaluating Contrast Gain	10
5 References	13
6 Acronyms List	13

## List of Figures

1	16 LWIR sensor + quad electro-optical (EO) prototype.	4
2	16 LWIR prototype camera calibration.	5
3	Camera positions during calibration: L- to the left of the centerline, 4.5m from the target; R - to the right of the centerline, 4.5m from the target; C - centerline, 7.4m from the target, F - centerline, 22 m from the target.	5
4	Images of the target as viewed by 4 RGB and 16 LWIR sensors.	6
5	LWIR Point Spread Function.	6
6	RGB Point Spread Function.	6
7	Image acquisition - the desert.	7
8	Image acquisition - the forest.	7
9	Preview of the nighttime captured LWIR footage as a binocular stereo (Butterfield Canyon, UT).	7
10	Preview of the daytime captured footage with RGB and LWIR sensors (Floras Lake, OR).	8
11	Single-scene disparity map generation: a) source thermal images; b) phase correlations for an image pair converged at infinity; c) multi-pair combination of phase correlations; d) disparity map by center-of-mass argmax of c); e) disparity map by Levenberg-Marquardt algorithm (LMA) argmax of b); f) full disparity map by LMA for disparity sweep.	9
12	Multi-scene disparity map generation: a) disparity map from the last (reference) scene in a sequence; b) outlines of the frames in a sequence; c) single-scene individual pair 2d correlations; d) single-scene multi-pair combination of phase correlations; e) single-pair combination of 2d correlations from all the 99 scenes; f) multi-scene multi-pair combination of phase correlations; g) disparity map generated from a scene sequence of the moving camera.	10
13	Captured image + noise.	10
14	Depth map with interscene accumulation: a) single-scene disparity maps for 2, 4, 8, and 16 sensors; b) 99-scene disparity maps; c) 99-scene disparity maps generated from the source images with added uncorrelated synthetic noise.	11
15	Disparity map quality vs. added synthetic noise: a) root mean square error (RMSE); b) density.	11
16	Contrast gains.	12

# 1 Project Summary

**Firm:** Elphel, Inc.

**Project Title:** Long Range Thermal 3D Perception in Low Contrast Environments

## 1.1 Identification and Significance of Innovation

Long-range 3D perception is an essential capability of the intelligent vehicle systems enabling situational awareness of the autonomous and piloted air vehicles for NASA AAM. Current depth sensing and exterior perception technologies are short-range automotive LiDARs and long-range radars with limited transversal and temporal resolution, especially in the dense urban environment, do not adequately respond to AAM requirements. High travel speeds combined with the relatively low deceleration rates require long sensing distances, and the range of the conventional LiDAR measurements is often insufficient. We propose to provide future air vehicles with LWIR 3D perception capability that enables vehicle awareness of the environment in degraded visual conditions, in the absence of ambient illumination, robust against GPS failure increasing the safety of National Air Space (NAS). Thermal images can be used similarly to the visible range ones for 3D scene reconstruction, but the challenges specific for LWIR - lower image resolution, lower contrast of the textures, and high thermal inertia, so far prevented its use for robust 3D. We have invented a novel method for thermal imaging contrast improvement over an order of magnitude, which will revolutionize thermal imaging and enable long-range 3D perception with uncooled LWIR sensors.

## 1.2 List of Technical Objectives

The main objectives of the Phase I project are to demonstrate  $10\times - 20\times$  improvement of the microbolometer-based LWIR detectors' system sensitivity and increase the ranging accuracy.

There were no available thermal image sets that we could use to evaluate the proposed technology, making such datasets acquisition our first objective. Our approach presents unique requirements for the captured data: a large number of synchronized non-collinear images (16 + 4 apertures) and strict requirements for the camera calibration (0.02pix reprojection RMSE). To achieve the objectives of Phase I, we assembled an experimental dual-modal (LWIR/EO) prototype system shown in Figure 1, acquired the representative image data sets, and implemented image processing algorithms to improve contrast with intrascene (using multiple simultaneous sensor images) and interscene (consolidating data from multiple consecutive scenes) methods.

We evaluated the contrast improvement as system NETD and compared it to the traditional stereo configuration and methods.

We expected to demonstrate  $4\times$  contrast improvement over the binocular configuration for the full 16-sensor scenes in this test, corresponding to the effective NETD of 10 mK. With the interscene accumulation, we planned to achieve a system NETD of 1 mK to 2 mK, depending on the number of accumulated scenes, camera movement, and the LWIR sensor module internal properties.

The above method and camera configuration allow developing a scalable Tradespace model, evaluating subsets of 2 (binocular), 4, 8, and all 16 sensors and comparing the achieved RMSE over the full scene FoV.

## 1.3 List of Technical Accomplishments

1. We have assembled the dual-modal (LWIR/EO) prototype camera, shown in Figure 1, for the experimental datasets' acquisition.
2. Performed photogrammetric camera calibration using our dedicated calibration setup with a large  $7\text{ m} \times 3\text{ m}$  LWIR/EO calibration pattern.
3. Acquired LWIR/EO image data sets in various field conditions to collect representative data.
4. Updated the software to accommodate processing from 16 LWIR simultaneously acquired images.
5. Evaluated thermal contrast improvement of 3D thermal perception system over the existing methods.
6. We have achieved the stated metrics of  $3.84\times$  increasing the contrast gain with the intrascene method and  $5.5\times$  additional contrast improvement with the interscene accumulation of measurements. Our results show 10.5 mK for intrascene and 1.9 mK with the interscene methods.
7. Our results prove the feasibility of the proposed technology.

## 1.4 Name and Address of Principal Investigator

Dr. Andrey Filippov

1455 West 2200 South #205, West Valley City, UT 84119, USA

## 1.5 Name and Address of Offeror

Elphel, Inc.

1455 West 2200 South #205, West Valley City, UT 84119, USA

## 2 Abstract

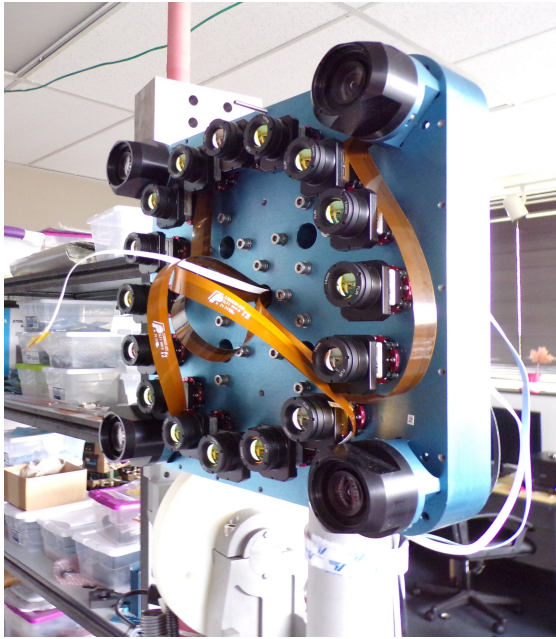


**Figure 1:** 16 LWIR sensor + quad EO prototype.

sensors. The conventional binocular stereo systems fail to fully use the image pair's captured data as only the mismatch along the epipolar lines contributes to the depth calculation. Our current research shows that even the quadocular stereo camera reduces effective NETD twice (not as  $\sqrt{2}$ ) compared to the binocular configuration, while the number of sensors is only two times higher. The 16-sensor prototype will improve effective NETD four times relative to a conventional binocular system, reaching 10 mK. Interscene accumulation of the 2D intrascene (single-shot) correlation output improves sensitivity by another order of magnitude.

## 3 Technical Objectives

The main research objective in Phase I is to prove the feasibility of dramatic (over an order of magnitude) improvement of the microbolometer-based LWIR detectors sensitivity, especially for the 3D measurements. This perception technology targets the critical for the AAM applications gap between currently available short-range automotive LiDARs and long-range radars with the limited transversal and temporal resolution, especially for the cluttered urban environment.

### 3.1 Approach

We will use a massive multi-aperture configuration of accurately calibrated uncooled LWIR sensors to enable 3D perception in extremely low-contrast environments at long range and high speed.

The proposed approach presents unique requirements for the captured data: a large number of the synchronized noncollinear images (preferably 16 or more) and strict requirements for the camera calibration (0.025pix reprojection RMSE) make achieving the project goals with currently available datasets impossible. We will use the data acquisition prototype designed and assembled as part of this research (Figure 1) to demonstrate an intrascene system NETD of 10 mK and reach 1 mK with the interscene accumulation for the environment's low-contrast features.

The LWIR subsystem containing sixteen FLIR Boson 640pix  $\times$  512pix camera cores (Figure 1) will provide image data to demonstrate system NETD<sup>1</sup> of 10 mK in the intrascene-only correlation mode. With the interscene accumulation possible for terrain (static) features with the initial software that is possible to upgrade for most moving objects, we expect to achieve system NETD of 1 mK to 2 mK depending on the number of accumulated scenes.

With the 32° horizontal field of view (HFOV) and 220 mm diameter of the lens centers circle, this small-size prototype will provide dense depth maps with 10 % accuracy at 500 m range using Phase I's preliminary software and disparity resolution of 0.05pix. In Phase II, we expect to improve disparity resolution to 0.025pix using a trained deep neural network (DNN) and achieve 5 % accuracy at 500 m.

The proposed effort aims to develop low SWaP-C day/night, all-weather depth-sensing hardware that can detect objects at far distances, e.g., 1500 ft to 3 nmi with passive LWIR sensors.

<sup>1</sup>The sensitivity of the hypothetical sensors in a binocular stereo configuration capable of ranging the same scene.

## 4 Technical Activities

### 4.1 Multi-Sensor Camera Assembly and Testing

To achieve the objectives of Phase 1, we assembled an experimental dual-modal (LWIR/EO) prototype system shown in Figure 1. We designed this system to use 16 identical microbolometer-based FLIR Boson camera cores (640pix  $\times$  512pix) evenly distributed over the circle of 110 mm radius and four 5 Mpixel RGB sensors positioned in the corners.

We have thoroughly tested these RGB sensors for long-range 3D sensing; they will provide ground truth measurements for thermal sensors during daytime operation. All the optical components are mounted on a 50 mm-thick base plate with an internal honeycomb structure to maintain the sensor modules' mechanical stability within 10  $\mu$ rad needed for 0.02pix disparity resolution of the 32° HFoV 640pix  $\times$  512pix thermal sensors. Each sensor module has a 3-axis attitude adjustment, enabling their alignment during the factory calibration procedure. While the differential rectification (DR) [1] method of image matching tolerates minor orientation errors, it still requires the imagers' mechanical alignment. In addition to the sensor components, the prototype system includes five Elphel NC393 quad-port camera system modules to acquire and record image data to the internal solid-state drive (SSD) devices. One such module operates four RGB sensors, and the other four control sixteen LWIR sensors (four each) and record images to the SSDs. Each sensor unit operates in the external trigger mode synchronized by the master camera. LWIR modules run at 60 Hz; the RGB ones capture 15 frames per second. The synchronization network distributes shared 1  $\mu$ s-accurate timestamps for embedding into each image file metadata, simplifying scene assembly from multiple storage devices.

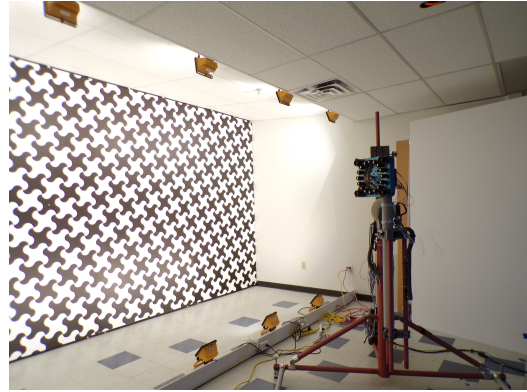


Figure 2: 16 LWIR prototype camera calibration.

### 4.2 Camera Calibration

Photogrammetric camera calibration is a precondition to achieve an accurate depth map in the stereo application, and most methods use dedicated calibration setups to perform this task.

We perform camera calibration with a large LWIR/RGB calibration pattern and goniometer for precise automatic rotation. Our dual-modality 7.0 m  $\times$  3.0 m calibration target consists of five separate panels fitted together. We use twelve 500 W halogen floodlights to illuminate the pattern printed on a 5 mm foamcore board glued to a 0.8 mm aluminum sheet. The forced airflow cools its back side.

The black-and-white pattern resembles the checkerboard one with each straight edge replaced by a combination of two arcs – this makes spatial spectrum uniform and facilitates point spread function (PSF) measurement.

We use an automated goniometer (Figure 2) to capture many (typically hundreds) image sets so that in captured data, each area of the camera sensor field of view (FoV) captures most of the large pattern. This allows accurate bundle adjustment to determine camera intrinsic and extrinsic parameters simultaneously with measuring the target pattern itself.

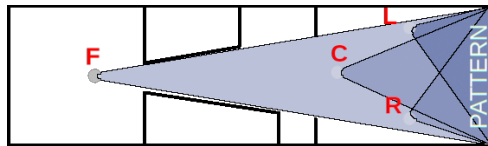


Figure 3: Camera positions during calibration: L- to the left of the centerline, 4.5m from the target; R - to the right of the centerline, 4.5m from the target; C - centerline, 7.4m from the target, F - centerline, 22 m from the target.

We captured image sets from 4 positions (“stations”) illustrated in Fig.3, accumulating 700 of them. Off-center stations (L and R) are needed for accurate measurement of the depth coordinate (target surface flatness), C is optimal for visible-range cameras PSF measurements (wide-angle view of the pattern but far enough for the depth of field (DOF)), and F is needed for the LWIR PSF measurements that have DOF limiting minimal fixed-focus distance to 20 m. Such a long distance is determined by a combination of large pixel-size (12  $\mu$ m), high lens numerical aperture (0.7), and a long focal length (14 mm).

It is not practical to build an “ideal” pattern with the accuracy sufficient for deep subpixel calibration, so instead, we measure the 3D location of each pattern grid node to approximately 0.1 mm accuracy. As a result of the calibration, we measure:

1. target pattern nodes coordinates;
2. each camera module radial distortion model parameters;
3. each camera module deviations from the radial distortion model;
4. each camera module location and orientation in the camera coordinate system;
5. space-variant point spread function (PSF) of each camera module for image aberration correction.

At each station, the goniometer scans the range of  $\pm 40^\circ$  horizontally and  $\pm 25^\circ$  vertically, so each pattern region covers each sensor's entire FoV.

We used all four stations data for bundle adjustment, then applied station C data to calculate PSF for the RGB cameras (Figure 6) and station F data to get LWIR PSF (Figure 5). Figure 4 illustrates the view of the target by all 20 sensors from station L, blog post [2] provides a video illustration of the calibration procedure.

The first step of processing calibration images is the extraction of the pattern grid from the individual images. First, software samples images in reverse binary order, then after finding a suitable candidate, it tries to expand the found area, adding nodes around. Curved pattern cells help eliminate false positives when the camera sees pattern reflection on the floor, especially strong for LWIR images. After determining the pattern area in the images, the software "refines" found pattern coordinates by generating a simulated pattern view for each captured image area by warping the ideal pattern to the second-degree local pattern distortion and calculating 2D correlation between the captured and simulated areas.

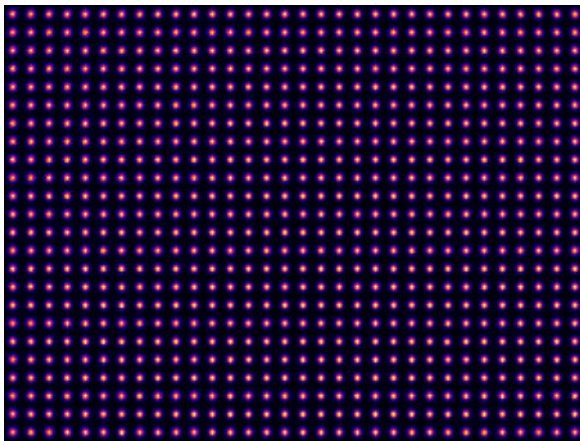


Figure 5: LWIR Point Spread Function.

from station C for RGB and station F for LWIR that contains a sufficiently large view of the target grid is used to calculate fragments of the whole PSF, as each image (especially for LWIR from station F) covers only a fraction of the entire FoV. These images are then combined (first outliers are removed, then remaining are combined in the frequency domain by separately averaging power spectrum and phase shifts), resulting in arrays of the space-variant PSF kernels shown in Figures 5,6.

The PSF kernels have twice higher resolution than the actual sensors (0.5 pix in each direction), and the distance between the kernels in these illustrations are not in scale with the image size, so the PSF full width in the center is less than 1.6pix compared to  $2592\text{pix} \times 1926\text{pix}$  of the full RGB images and  $640\text{pix} \times 512\text{pix}$  of the LWIR ones. Color channels of RGB images are processed separately; Figure 6 combines them, revealing the chromatic aberration.

We then invert the PSF kernels to get deconvolution kernels needed for aberration correction of the field-acquired images.

### 4.3 Field Image Acquisition

We have captured both daytime dual-modal (LWIR + EO) image sets (Figure 10) and nighttime LWIR-only ones (Figure 9) using our backpack-mounted platform in various environments (as shown in Figure 7 and Figure 8). RGB images

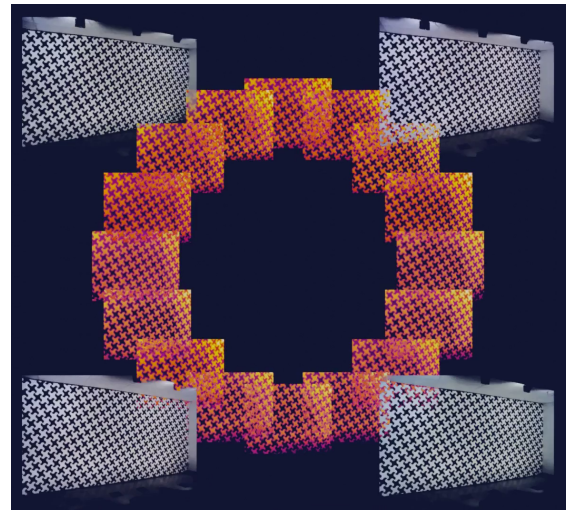


Figure 4: Images of the target as viewed by 4 RGB and 16 LWIR sensors.

This processing results in a set of subpixel-accurate floating point coordinates of the pattern grid nodes; we save this data as multi-layer TIFF files ("grid files") that are convenient to evaluate manually.

We process grid files generated from the captured images (700 scenes of 20 images each) with an LMA simultaneously adjusting 3-5 thousand parameters using 5-10 million points (measured X/Y positions of the pattern grid nodes), resulting in RMSE under 0.05 pix. With radial distortion alone (without non-radial deviations correction), the RMSE is 0.12-0.15 pix, proving the more advanced processing required to achieve needed calibration accuracy, the processing we implemented in our work.

The next step after distortions calculation is measuring the space-variant PSF by combining partial arrays, each covering a fraction of the entire sensor FoV. Each image captured



Figure 6: RGB Point Spread Function.

from EO cameras have a much higher resolution ( $2592\text{pix} \times 1936\text{pix}$  vs.  $640\text{pix} \times 512\text{pix}$ ) than LWIR images, allowing us to use RGB images as ground truth data for evaluation of the LWIR-derived depth map accuracy and training and testing of the DNN.



**Figure 7:** Image acquisition - the desert.

Each recording session (0.5-1.0 hours long) resulted in several hundred gigabytes of raw data and about a million individual images. We created preview videos from the raw data files to simplify selecting initial scene sequences for further processing. These files are much smaller and we were able to upload them to our web server - they are now available in subfolders of <https://community.elphel.com/files/lwir16/>.

Each of the three series contains individual channel videos: chn\_00.webm to chn\_15.webm for LWIR channels and chn\_16.webm to chn\_19.webm for the RGB ones (RGB channels are available for floras\_lake only, orford and butterfield are captured at nighttime without any meaningful RGB data). Videos are rendered at constant 30 fps, so continuously captured segments look as slow motion, and the missing 3 s gaps result in “jumps” in the video.

Each image frame has a visible timestamp that matches the filename of the raw image. The LWIR channels numbers start from the top (channel 0); other channels are located clockwise, looking in the direction parallel to the camera view. RGB channels are top-left (16), top-right (17) bottom-left (18) and bottom-right (19). In addition to the videos, we created simple viewers to watch stereo-pairs of images (just captured images without any correction) using Google cardboard stereo-viewer or a similar device.

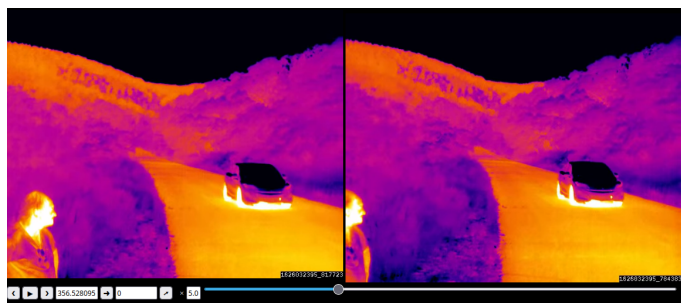


**Figure 9:** Preview of the nighttime captured LWIR footage as a binocular stereo (Butterfield Canyon, UT).

#### Floras Lake, Oregon

- [floras\\_lake/video-1-15.html](#)
- [floras\\_lake/video-2-14.html](#)
- [floras\\_lake/video-3-13.html](#)
- [floras\\_lake/video-4-12.html](#)
- [floras\\_lake/video-17-16.html](#) – a stereo-pair of RGB videos (frame size is twice reduced, each frame is repeated six times to match LWIR)
- [floras\\_lake/video-14-16.html](#) – not a stereo-pair, just a side-by-side comparison of RGB and LWIR videos.

Due to the limitation of the current camera field-programmable gate array (FPGA) code that lacks lossless compression of 16-bit thermal images and bandwidth limitations of the simultaneous 4-channel LWIR data recording and our need to capture long image sequences at a full frame rate for interscene contrast improvement, we implemented a special “burst” recording mode. Periodically, each camera module simultaneously acquires consecutive images at maximal frames per second (FPS), filling corresponding RAM buffers (64 MB per channel). One burst lasts 1.67 s allowing recording of 100 consecutive LWIR images at 60 Hz (17 images of RGB images recorded at 10 Hz); and after a 3 s pause, the sequence repeats. We record the synchronized sequence of JP4-encoded RGB images and 16-bit TIFF LWIR images enclosed in 1 GB \*.mov files, reducing the number of individual files.



**Figure 8:** Image acquisition - the forest.

#### Port Orford, Oregon

- [orford/video-1-15.html](#) – two near-top images at approximately the human eye distance (the smallest stereo disparity)
- [orford/video-2-14.html](#)
- [orford/video-3-13.html](#)
- [orford/video-4-12.html](#) – pair of the most distant cameras (the largest stereo disparity)

#### Butterfield Canyon, Utah

- [butterfield/video-1-15.html](#)
- [butterfield/video-2-14.html](#)
- [butterfield/video-3-13.html](#)
- [butterfield/video-4-12.html](#)

We created these images for scenes preview and selection only; they are not a part of the image processing flow.

#### 4.4 Extending Software to Support Arbitrary Number of Sensors

Our previously developed image-processing and 3D-reconstruction software that we have been developing since 2017 specifically depended on a quadocular camera configuration with four sensors located at the corners of a square. Such layout allowed the simple fusion of the horizontal stereo-pairs with the vertical ones by a lossless transposing of the 2D phase correlation outputs. For the larger number of cameras, we needed rotation by almost arbitrary angles and scaling of the phase correlation outputs to combine results of the correlations with various baselines – from 1/5 of the diameter ( $\sin(\pi/16)$ ) for the neighboring sensors to the full diameter. We accomplished this by developing different methods of multi-pair consolidation of the 2d correlation and refactoring the code to support an arbitrary number of sensors.

One of the first functions of the updated code tested for 16-sensors scenes (simultaneously captured sets of LWIR images) was the code for field calibration (“Lazy Eye” correction - [ExtrinsicAdjustment.java](#)) to measure and compensate for minor misalignment of the sensor modules that may develop over time or caused by vibrations or mechanical distortions caused by temperature variations. While we did not yet process a massive number of captured scenes to calculate statistical properties of the required correction amounts, selective processing of the image sets captured at different locations (described in subsection 4.3) confirmed that the misalignment of the sensors is below 0.1pix and verified the overall mechanical stability of the prototype system (Figure 1).

#### 4.5 Generating a Single-Scene Disparity Map

Single-scene generation of the disparity map with the multi-sensor camera is an iterative process that resembles human stereo-vision involving eye convergence followed by processing the residual mismatch between the two registered images. In our case, pre-shifting corresponding image tiles before calculating the 2d phase correlations replaces mechanical eyes movement. The mechanical movement of the eyes is substituted by pre-shifting corresponding image tiles before calculating the 2d phase correlations. The calculation of the pairwise correlation between corresponding image tiles requires significant overlap between the registered images, and the correlation result quickly degrades when tile overlap reaches its half-width. The iterative process starts from some initial approximation of the disparity map referenced to a virtual camera positioned in the center of the sensor circle. According to the DR method, this virtual camera has the optical distortions averaged from the measured during factory calibration distortions of the sensors. The initial approximation may be obtained by a full disparity sweep, prediction from the previous scene, expanding from the known areas, or other algorithms. These initial generalized disparity values are reciprocal to the object distances for each tile center on a uniform grid (stride 8) of the virtual camera. For the traditional binocular stereo, it will be the actual shift between the two images in pixels. In the multi-sensor case, this single for each tile scalar value is used to calculate a vector that indicates how each image should be shifted to match the other ones. For a circular camera configuration, this vector has the same length with the direction matching the camera’s location. The exact vector calculation uses the calibration results and compensates for measured misalignments and distortion differences.

Knowing these 16 vectors, we implement the required pre-shift in two steps:

- round the shift to the nearest integer and use it to select a  $16 \times 16$  corresponding tile in each source image, and
- apply the residual  $\pm 0.5$ pix shift as a lossless rotation in the [Frequency Domain \(FD\)](#).

The [Tile Processor \(TP\)](#) operates on each tile independently (and in parallel when implemented in [graphics processing unit \(GPU\)](#) or custom hardware), starting with the conversion to the [FD](#), correction of the optical aberrations by the deconvolution with the known from the factory calibration kernels, applying calculated fraction-pixel shift by complex values rotation and calculating the 2d phase correlations. In the current work, we calculated all 120 sensor pairs, leaving the reduction of this number for future effort. The calculation of the phase correlation involves the normalization of the [FD](#) representation by dividing each complex value of the 2d array by its absolute value. In the noiseless case, this would lead to a sharp 2d  $\delta$ -function when converted back to the pixel domain, but it would amplify noise and make it difficult to find the correlation maximum and thus the disparity. This noise amplification is mitigated by adding a small constant to the absolute value (a “fat zero”) in the denominator during normalization, balancing between low noise/wide maximum (regular correlation for a high value of the fat zero) and high noise/sharp maximum (pure phase correlation for “fat zero” equals zero).



**Figure 10:** Preview of the daytime captured footage with RGB and LWIR sensors (Floras Lake, OR).

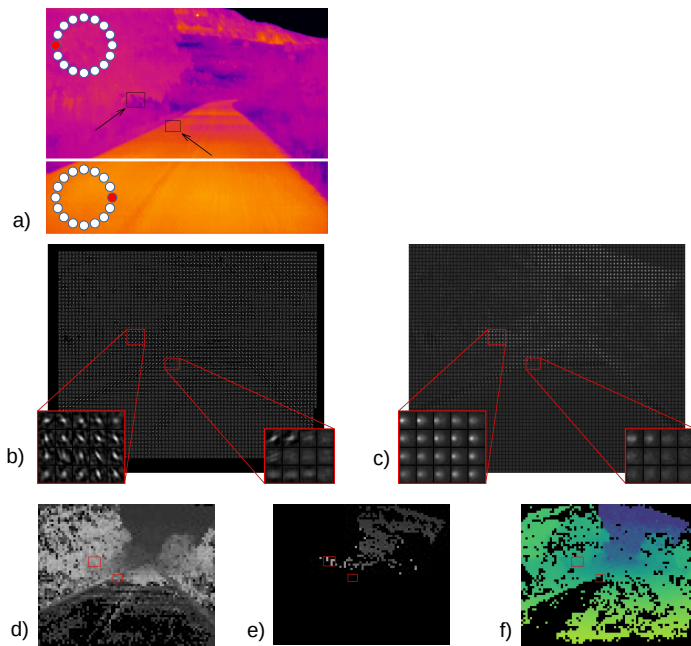


**Figure 11:** Single-scene disparity map generation: a) source thermal images; b) phase correlations for an image pair converged at infinity; c) multi-pair combination of phase correlations; d) disparity map by center-of-mass argmax of c); e) disparity map by LMA argmax of b); f) full disparity map by LMA for disparity sweep.

scaled to align the disparity vectors, and then accumulated. The result loses shape information (helpful in following object edges) but provides an easy method to combine correlation outputs and increase [signal-to-noise ratio \(SNR\)](#) before looking for an argmax.

As the 11b is calculated with zero pre-shift (“eyes” are converged at infinity) the 11c outputs meaningful results only for distant objects with the disparity of less than approximately 4 pixels. The 11d shows this residual disparity measured by a center-of-mass method applied to 11c and results in false disparity for the highway pavement in the bottom part of the image (as if it is much farther than the pavement representation above it). The 11e outputs the result of the LMA fitting applied directly to all 120 partial correlations of 11c (bypassing averaging in 11c). It uses more pessimistic filtering that discards low confidence tiles and requires fewer iterations to achieve the same depth accuracy. The last subplot – 11f provides a full disparity map resulting from the iterative process of disparity refinement after the initial disparity sweep. It also tries to fill the gaps caused by the low-contrast areas by reducing lateral resolution and consolidating multiple neighboring tiles, assuming that low-contrast usually assumes that the corresponding surface in 3d is flat or near-flat. There are still some gaps in the disparity map (black) remaining, and the following subsection describes how to boost contrast by interscene accumulation of the intrascene correlation results.

#### 4.6 Generating a Disparity Map from a Scene Sequence

The interscene accumulation is based on an observation that most of the low-contrast objects of the scene, such as rocks, bushes, potholes on the road, are static in 3D, while the moving objects (people, animals, machinery) have high thermal contrast that allows their robust detection and ranging. There are certain situations where moving objects may also have low thermal contrast, and we plan to implement interscene accumulation of such objects in Phase II by extending image processing capabilities to compensate for their movement.

The final real-time implementation will optimize processing to reduce the number of calculations for each newly acquired scene (use incremental 3D model generation). However, the current research only aims to enhance contrast and depth accuracy of the last acquired (reference) scene number 99, using previous scenes (1 to 98) for that purpose.

The interscene accumulation process starts with building partial disparity maps for all scenes in a sequence described in the previous Subsection 4.5. Figure 12a illustrates the partial disparity map of a reference scene. The software scans all the subsequent scene pairs: reference (99) and the previous 98, 98 and 97, up to 2 and 1. It fits each pair’s partial disparity map using per-tile 2D correlations (reusing the same low-level methods as for image correlation) and results in the camera linear movement and rotation 6-element vector. At this iteration, we only compare subsequent scenes (1/60 of a second apart) as they differ little from each other, making correlation simple. For matching, we use each scene “disparity confidence” available for each scene in addition to the disparity itself and an output from the high-pass filter

Calculation of the correlation maximum (*argmax* function) determines the relative distance to the object (a voxel of the depth map); this residual disparity is added to the initial disparity estimation. The process repeats until the change in disparity falls below a specified threshold. This iterative procedure provides high accuracy of the disparity calculation achieving deep subpixel resolution because while pre-shifting in the FD is lossless, measurement of the residual disparity is prone to pixel-locking (Fincham and Spedding [3]) effect that distorts the results.

Figure 11 illustrates a single-scene disparity map calculation. The 16 thermal images of 11a provide input; the horizontal split shows a disparity between the images from the leftmost sensor (top) and the rightmost (bottom). The two black rectangles indicate the high-contrast and low-contrast areas. Figure 11b shows one of the 120 pairwise phase correlations. When the tile corresponds to an object at the same distance, each of its 120 correlations has the elliptic shape of the same size/orientation with its center shifted from the tile center proportional to the vector that connects lens centers. One of the simple methods that combine multiple correlation tiles results in 11c. Each partial correlation output is rotated and

from the down-scaled source thermal images. During this iterative process, we re-calculate the predicted appearance of the other scene from the reference scene camera position, use per-tile correlation to measure X and Y offsets for each tile, and then fit a 6-element global camera movement vector with **LMA**.

Having built pairwise scene camera ego-motion vectors, we perform a second pass to calculate relative camera positions at each scene to the reference one (97 to 99, 96 to 99, ..., 1 to 99). Just a multiplication of the pairwise matrices would accumulate errors, but we can use them in the iterative process. Consider, we have already referenced scene 51 to the 99. We can multiply the available pairwise movement matrix from scene 50 to 51 and from 51 to 99, then use it as an initial approximation of 50 to 99 movement and improve accuracy by the direct correlation between scenes 50 and 99, and repeat this algorithm until all scenes camera positions are referenced to the scene 99. Figure 12b illustrates this by showing a stack of offset scene images under reference scene one.

Individual depth maps 12a are filtered and averaged (avoiding averaging the foreground with background elements) with disparity gaps filled by predictions resulting in a dense (defined for every tile of the reference scene) but maybe inaccurate disparity map to be enhanced later by the simultaneous correlations processing.

Then we calculate pairwise correlations for each scene, but this time each image tile center's locations are calculated to match reference scene tiles, not the tiles of the virtual image of that scene as we did before. Figures 12c and d represent single-pair phase correlations and their combinations, respectively, similar to earlier Figures 11b and c. The difference is that this time the full-scene pre-shift based on the known disparity map is applied, so each tile phase correlation output is centered. The later steps do not use single-scene 12b and c; they are only provided for comparison. Instead, the **FD** representation of the correlation (still as complex values, not collapsed by the transformation to the pixel domain) are averaged among the same tile pair in all scenes where the corresponding object is visible (it is present in the **FoV** and not occluded). We apply the non-linear step of amplitude normalization followed by the inverse transformation only once after averaging preserving **SNR** increase as a square root of the number of independent measurements even when it is much less than 1.0 in the individual scenes.

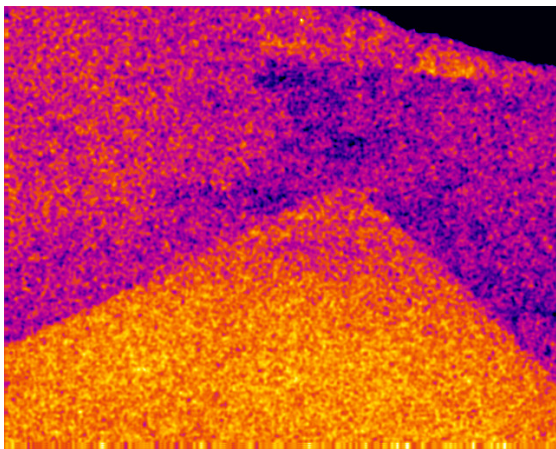


**Figure 13:** Captured image + noise.

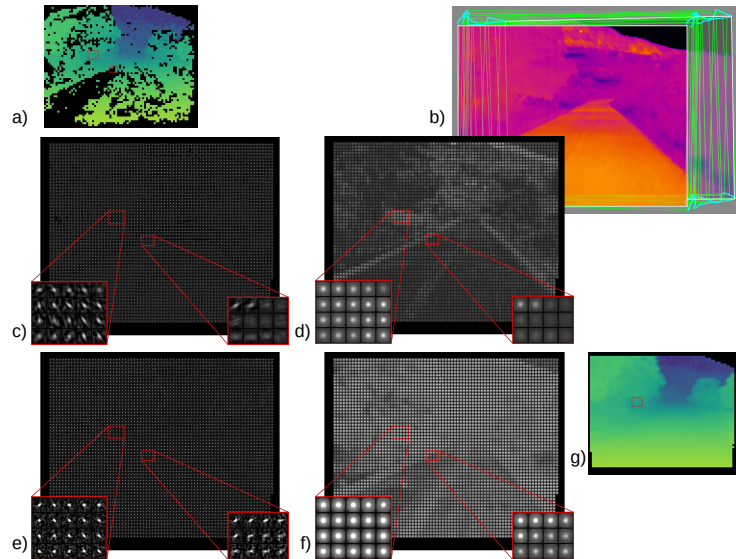


**Figure 12:** Multi-scene disparity map generation: a) disparity map from the last (reference) scene in a sequence; b) outlines of the frames in a sequence; c) single-scene individual pair 2d correlations; d) single-scene multi-pair combination of phase correlations; e) single-pair combination of 2d correlations from all the 99 scenes; f) multi-scene multi-pair combination of phase correlations; g) disparity map generated from a scene sequence of the moving camera.

Figure 12e illustrates individual pair phase correlations and 12f) – a combination of all 120 pairs for a center-of-mass argmax calculation. More accurate **LMA** fitting uses individual pairs of 12e. We will feed these shape-preserving per-pair phase correlation outputs to the **DNN** as we did with a quad-camera in previous research.

#### 4.7 Evaluating Contrast Gain

When we obtained dense disparity maps using captured thermal images from all available (16) sensors, we needed to evaluate the influence of the number of sensors and the contribution of interscene accumulation. Setting up a “fair competition” between different sensor configurations is not a trivial task because the complete procedure of calculating the depth map from the sequence of the captured thermal images involves multiple non-linear processing stages depending on a large number of parameters. It would be extremely difficult to explore and optimize all the parameter space for each of them and to guarantee

that we are comparing optimized for binocular to optimized for quadocular, and the same for a higher number of sensors.

To resolve this challenge, we tried to narrow the “competition” task and reduce the number of independent parameters that influence the quality of the depth map output.

We started with the best depth map we could achieve using all scenes and all sensors, considering it to be the best approximation of the ground truth. Then we added the same constant value (it is currently 1.4142 pixels) to all tiles and used this offset depth map as initial pre-shift (equivalent to “eye convergence”) before calculating the first iteration of the per-tile phase correlation. Then we performed a fixed number (10) of disparity refinement iterations of measuring residual disparity from argmax of combined correlations, adding it to disparity estimation (pre-shift) and re-calculating correlations.

Each tile disparity value was either converging to a final value (last step typically under  $1 \times 10^{-5}$ pix) or diverging. Furthermore, if converging, the disparity could be close to the expected value (obtained from 99 scenes, 16 sensors) or far. We considered tiles with the final error above 2.0pix as “diverged” (reducing calculated map density) and calculated **RMSE** only for the converged ones.

For this test, we used only center-of-mass argmax as it does not depend on any configuration parameters, while the more advanced **LMA**-based method depends on them. The center-of-mass method provides “confidence” output, but its interpretation depends on different heuristic thresholds for different configurations, so we did not filter depth map outputs from outliers, visible in Figure 14. The only remaining parameter that influences the result is phase correlation “fat zero,” and we verified that changing it twice (both ways) from the selected value did not significantly affect any configurations. The amount of initial offset (1.4142) has to be significantly smaller than minimal tile overlap ( $\approx 4$ ) and larger than the maximal **RMSE** we expected to measure.

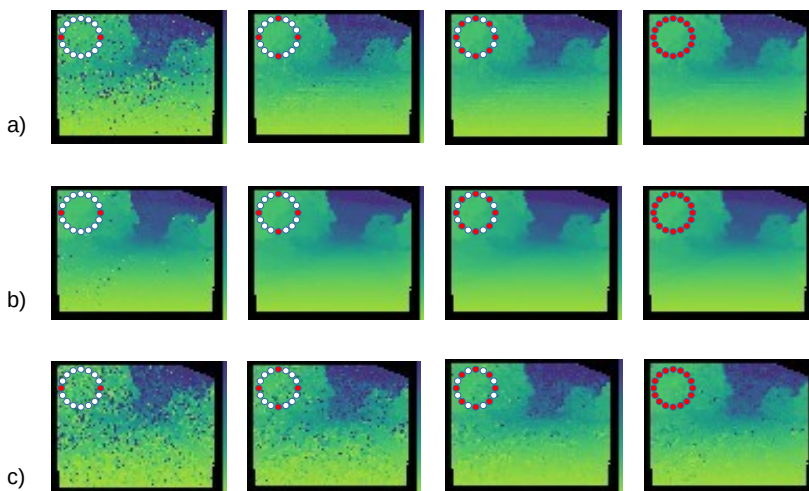


**Figure 14:** Depth map with interscene accumulation: a) single-scene disparity maps for 2, 4, 8, and 16 sensors; b) 99-scene disparity maps; c) 99-scene disparity maps generated from the source images with added uncorrelated synthetic noise.

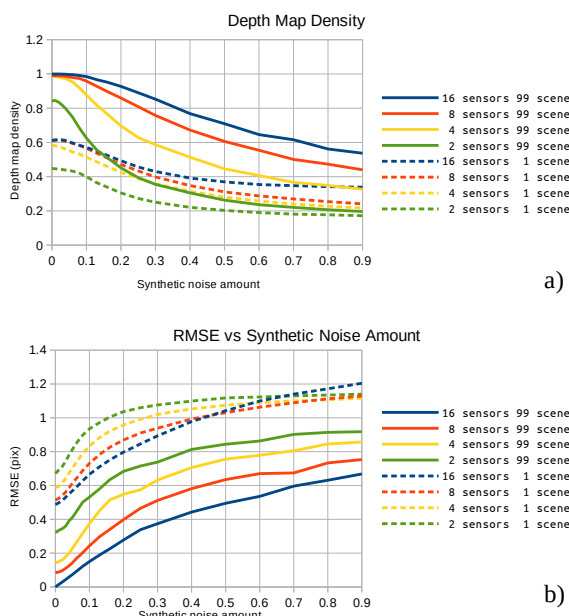


**Figure 15:** Disparity map quality vs. added synthetic noise: a) **RMSE**; b) density.

0.01pix) and differed from the expected value by less than 2.0pix. The **RMSE** shown in Figure 15a excludes diverged

Figure 14a shows the resulting depth maps for single-scene 2, 4, 8, and all 16 sensors; 14b – same for interscene accumulation. The thermal images we used were acquired only two hours after sunset and had significant contrast, so the interscene results (Figure 14b) were almost identical for 4, 8, and 16 sensors. To reveal the difference, we added synthetic noise of variable amplitude to the source images, such as in Figure 13 (amplitude of 0.3 of the entire pixel range captured), and used it to generate Figure 14c.

The software generated synthetic noise images for each scene, each sensor once, saved and then mixed to the captured images, so each sensor configuration got the same input data.

We used the following simplified model to compare the performance of different sensor configurations quantitatively. Each sensor has the same intrinsic noise, invariant of the pixel position in the field of view. The 3d scene element corresponding to each tile of the reference scene defines its useful signal. Different sensor configurations have different signal gains, and the outcome of the disparity calculation for each tile depends on the **SNR** for that tile. During this procedure, we applied different amounts of synthetic noise, measuring depth map density and **RMSE**. Depth map density shown in Figure 15a is a fraction of all tiles for which the repetition of ten cycles of disparity refinement converged (to less than

tiles. The single-scene graphs (plotted with dashed lines) represent averaging of 16 instances of noise files of the same amplitude and have less random fluctuations than those for the interscene results (solid lines), each representing just a single set of noise files (because of very high calculation time).

According to the used model, the individual plots should differ by a horizontal scaling factor with the offset (for noise squares) of the intrinsic noise of the physical sensor that is still present when there is no synthetic noise. The simplified model is not very accurate, e.g. the **RMSE** plot for 16-sensor interscene intersects that of 8-sensor one at the relative noise level of 0.4 while the corresponding density falls at a lower rate than for the other number of sensors. That can be explained as that higher number of sensors locks to a larger variety of different objects correlation tiles present in the scene and fail gracefully by just an increased **RMSE** rather than by a complete divergence.

Figure 16 represents ratios of the inverted functions of Figure 15, ratios of the synthetic noise levels for the same values of the **RMSE** (a, c, and e), and map density (b, d, and f). The result contrast improvements for different numbers of sensors is calculated from combined data of 15c and 15d and the interscene gain – from 15e and 15f by averaging the contrast ratios (vertical axes). The amount of intrinsic sensor noise (optimal value is 0.044) is determined by minimizing the spread of the contrast gains.

We expected the intrascene contrast gain to be proportional to a square root of the independent number of stereo-pairs; this number is 1 for binocular and equals the number of sensors for other configurations where each sensor image contributes to two orthogonal stereo-pairs. These orthogonal pairs are independent measurements of the average disparity as for each pair matching only image shift parallel to the corresponding baseline contributes to the output. The measured results (presented in Table 1) for intrascene contrast gain are close to the predicted. The interscene accumulation should result in up to a square root of the number of measurements ( $10\times$  for 99 scenes), and so far, we achieved only  $5.5\times$  gain. Part of the lower gain is caused by insufficient scene overlap that reduces the number of measurements per tile. Another part may be caused by the manufacture-proprietary image processing inside the sensor that introduces a dependency between consecutive images. We will conduct more experiments to pinpoint this discrepancy’s reasons.

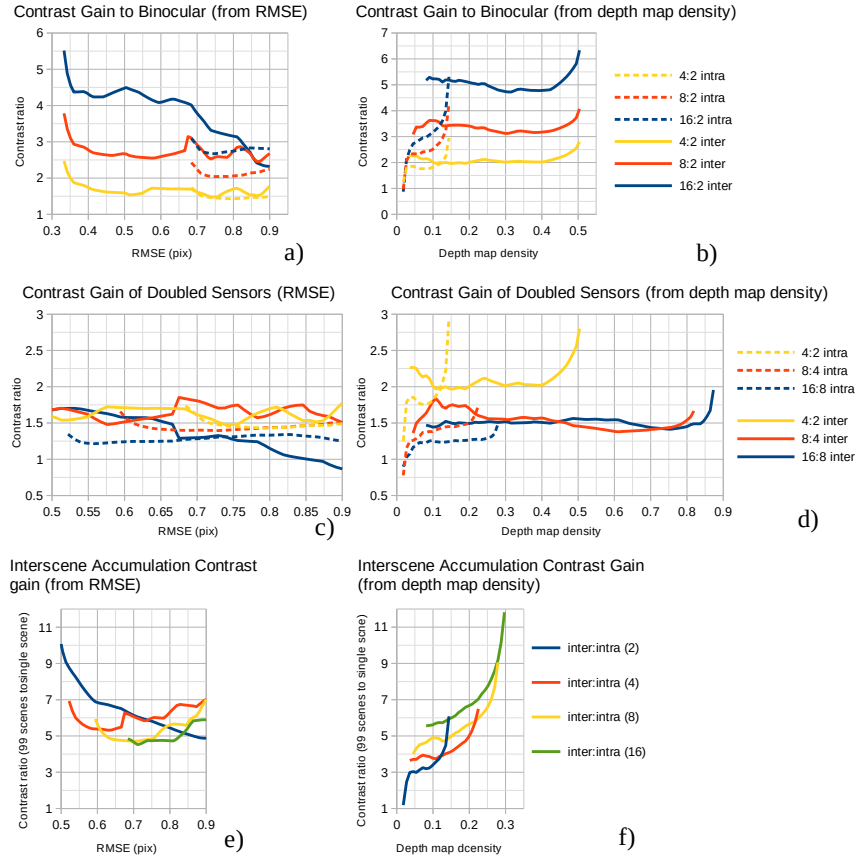


Figure 16: Contrast gains.

Table 1: Contrast Gain over Single-Scene Binocular Stereo

Configuration	Measured Gain	Predicted Gain
4-sensor over binocular	1.79	2.0
8-sensor over binocular	2.72	2.83
16-sensor over binocular	3.84	4.0
99-scene over single scene	5.5	9.95
99-scene, 16 sensor over single scene binocular	21.1	39.8

Using measured contrast values, we can calculate the effective system **NETD** – required thermal sensitivity of a pair of hypothetical thermal sensors in a traditional binocular stereo configuration (without interscene accumulation) to achieve the same depth map density and accuracy as a multi-sensor system build of 40 mK **LWIR** image sensors.

**Table 2:** Effective System **NETD**

Number of Scenes	Binocular	4-Sensor	8-Sensor	16-Sensor
1	40.0 mK	22.4 mK	14.7 mK	10.5 mK
99	7.3 mK	4.1 mK	2.71 mK	1.9 mK

## 5 References

- [1] A. Filippov, "Method for the FPGA-based long range multi-view stereo with differential image rectification," Apr. 28 2020. US Patent 10,638,109 B2. 5
- [2] A. Filippov, "Calibration of the LWIR16 camera prototype." <https://blog.elphel.com/2021/07/calibration-of-the-lwir16-camera-prototype>, 2019. Technical blog post. 6
- [3] A. Fincham and G. Spedding, "Low cost, high resolution DPIV for measurement of turbulent fluid flow," *Experiments in Fluids*, vol. 23, no. 6, pp. 449–462, 1997. 9

## 6 Acronyms List

- AAM** Advanced Air Mobility 1, 3, 4
- COTS** commercial off-the-shelf 1
- DNN** deep neural network 4, 7, 10
- DOF** depth of field 5
- DR** differential rectification of the stereo images to the common for the set distortion model 5, 8
- EO** visible range electro-optical imaging system 2–7
- FD** Frequency Domain, usually same as Transform Domain - data transformed by Fourier or similar transform, enables efficient implementation of convolution and correlation 8–10
- FoV** field of view 5, 6, 10
- FPGA** field-programmable gate array 7
- FPS** frames per second 7
- GPS** Global Positioning System 1, 3
- GPU** graphic processing unit, used for massively parallel processing, including ML 8
- HFoV** horizontal field of view 4, 5
- LiDAR** light detection and ranging 3, 4
- LMA** Levenberg-Marquardt algorithm 2, 6, 9–11
- LWIR** long wave infrared (8-15  $\mu\text{m}$ ) 1–8, 12
- ML** machine learning 13
- NAS** National Air Space 3
- NETD** noise-equivalent temperature difference 1, 3, 4, 12, 13
- PSF** point spread function 5, 6
- RMSE** root mean square error 2–4, 6, 11, 12
- RTL** register-transfer level - design abstraction level in hardware description languages 13
- SNR** signal-to-noise ratio 9–11
- SSD** solid-state drive 5
- SWaP-C** size, weight, power, and cost 1
- TP** Tile Processor - Elphel software/register-transfer level (RTL) for transform-domain image processing 8